RSC Publishing Faraday Discussions

Effects of symmetry breaking on the translation-rotation eigenstates of H2, HF, and H2O inside the fullerene C60

Journal:	*Faraday Discussions*
Manuscript ID	FD-ART-04-2018-000082.R1
Article Type:	Paper
Date Submitted by the Author:	11-May-2018

Complete List of Authors:	Bacic, Zlatko; New York University, Department of Chemistry; NYU-ECNU Center for Computational Chemistry at NYU Shanghai, 3663 Zhongshan Road North Vlcek, Vojtech; University of California, Los Angeles, Department of Chemistry and Biochemistry Neuhauser, Daniel; UCLA, Chemistry Felker, Peter; University of California, Los Angeles, Chemistry & Biochemistry

SCHOLARONE™
Manuscripts

Journal Name

ARTICLE TYPE

Cite this: DOI: 10.1039/xxxxxxxxxx

Effects of symmetry breaking on the translation-rotation eigenstates of H_2, HF, and H_2O inside the fullerene C_{60} †

Zlatko Bačić,*[ab] Vojtěch Vlček,[c] Daniel Neuhauser[c] and Peter M. Felker*[c]

Received Date
Accepted Date

DOI: 10.1039/xxxxxxxxxx

www.rsc.org/journalname

Splittings of the translation-rotation (TR) eigenstates of the solid light-molecule endofullerenes M@C_{60} (M = H_2, H_2O, HF) attributed to the symmetry breaking have been observed in the infrared (IR) and inelastic neutron scattering spectra of these species in the past couple of years. In the recent paper [Felker *et al., Phys. Chem. Chem. Phys.*, 2017, **19**, 31274], we established that the electrostatic, quadrupolar interaction between the guest molecule M and the twelve nearest-neighbor C_{60} cages of the solid is the main source of the symmetry breaking. The splittings of the three-fold degenerate ground states of the endohedral *ortho*-H_2, *ortho*-H_2O and the $j = 1$ level of HF calculated using this model were found to be in excellent agreement with the experimental results. Utilizing the same electrostatic model, this theoretical study investigates the effects of the symmetry breaking on the excited TR eigenstates of the three species, and how they manifest in their simulated low-temperature (5-6 K) near-IR (NIR) and far-IR (FIR) spectra. The TR eigenstates are calculated variationally for both the major P and minor H crystal orientations. For the H orientation, the calculated splittings of all the TR levels of these species are less than 0.1 cm^{-1}. For the dominant P orientation, the splittings vary strongly depending on the character of the excitations involved. In all the species, the splittings of the higher rotationally excited levels are comparable in magnitude to those for the $j = 1$ levels. For the levels corresponding to purely translational excitations, the calculated splittings are about an order of magnitude smaller than those of the purely rotational eigenstates. Based on the computed TR eigenstates, the low-temperature NIR (for M = H_2) and FIR (for M = HF, H_2O) spectra are simulated for both the P and H orientations, and also combined as their weighted sum (0.15H + 0.85P). The weighted-sum spectra computed for M = H_2 and HF match quantitatively the corresponding measured spectra, while for M = H_2O the weighted-sum FIR spectrum predicts features that can potentially be observed experimentally.

1 Introduction

From the moment it was serendipitously discovered by Kroto *et al.*,[1] C_{60} has captured the attention and imagination of scientists, as well as general public, owing to its exceptionally high symmetry and unsurpassed elegance. Immediately apparent was also the unique potential of C_{60} and other fullerenes for encapsulating atoms and molecules in their interior cavity, and exploring the unusual behavior of the (largely) isolated guest species in a homogeneous nanoscale confinement.[1] Supramolecular complexes in which a light molecule M is trapped inside the fullerene cage are referred to as light-molecule endofullerenes,[2] and denoted by M@fullerene. The synthesis of light-molecule endofullerenes in macroscopic quantities became possible by the procedure known as molecular surgery,[3–5] in which an opening is created in the fullerene through a series of organic reactions allowing the insertion of the guest molecule, after which the hole is closed and the original fullerene shell restored, encapsulating the molecule permanently in the cage interior. Using this approach, in little more than a decade three light-molecule endofullerenes have been synthesized, H_2@C_{60},[6,7] H_2O@C_{60},[8] and most recently HF@C_{60}.[9] It should be noted that the large cavity of C_{70} has allowed the encapsulation of not just one but two guest molecules, H_2 and H_2O, respectively, inside the cage of the larger fullerene C_{70}, resulting in the extraordinary endofullerenes

[a] *Department of Chemistry, New York University, New York, NY, 10003, USA; E-mail: zlatko.bacic@nyu.edu*
[b] *NYU-ECNU Center for Computational Chemistry at NYU Shanghai, 3663 Zhongshan Road North, Shanghai, 200062, China.*
[c] *Department of Chemistry and Biochemistry, University of California, Los Angeles, CA 90095-1569, USA; E-mail: felker@chem.ucla.edu*
† Electronic Supplementary Information (ESI) available: [details of any supplementary information available should be included here]. See DOI: 10.1039/b000000x/

This journal is © The Royal Society of Chemistry [year]

$(H_2)_2@C_{70}$[10] and $(H_2O)_2@C_{70}$.[11] It has even proved possible to encapsulate simultaneously two different molecules, H_2O and HF, in the interior of C_{70}, yielding the unprecedented mixed endofullerene $(H_2O{\cdot}HF)@C_{70}$.[12]

The most conspicuous feature of the light-molecule endofullerenes $M@C_{60}$ (M = H_2, H_2O, HF) is the dominance of quantum effects in the dynamics of the guest molecule,[13,14] particularly for the low temperatures (typically ranging from 1.5 K to about 30 K) at which the spectroscopic measurements on $M@C_{60}$ are usually carried out. As described in the following, the $M@C_{60}$ endofullerenes manifest a number of most basic tenets of quantum mechanics, to a degree, and with the clarity, unparalleled among molecular systems. The strong quantum effects arise from the quantization of the translational center-of-mass (c.m.) degrees of freedom of M due to its tight confinement inside C_{60} (particle-in-a-box effect) and low molecular mass, resulting in eigenstates whose energy differences are large relative to kT (where k is the Boltzmann constant). The quantized rotational states are well separated in energy as well, since the rotational constants of these molecules are large. Finally, the quantized translational and rotational motions of M are coupled by the interior surface of C_{60}, giving rise to a sparse translation-rotation (TR) (or "rattling") energy level structure, which nevertheless has the fingerprints of the surprisingly rich and intricate quantum dynamics outlined below.

Additional quantum features in the TR dynamics appear when M has two symmetrically equivalent ^{1}H nuclei (e.g., H_2 and H_2O), that are fermions since their nuclear spin is 1/2.[2] Then, in order to satisfy the Pauli principle, the total molecular wave function of M, its spatial and spin components, must be antisymmetric with respect to the exchange of the two fermions. This requirement entangles the spin and spatial quantum states in a particular way, leading to nuclear spin isomers, *para* and *ortho*, of both H_2 and H_2O, having total nuclear spins $I = 0$ and 1, respectively. For *para*-H_2, only even-j rotational levels are allowed ($j = 0,2,\ldots$), while *ortho*-H_2 occupies only odd-j rotational levels ($j = 1,3,\ldots$), j being the rotational quantum number of the diatomic molecule. The rotational states of H_2O are conventionally labelled with the asymmetric top quantum numbers $j_{k_a k_c}$; for *para*-H_2O, $k_a + k_c$ has even parity, while for *ortho*-H_2O, $k_a + k_c$ has odd parity.[15] This entanglement of the rotational and nuclear-spin states makes the already sparse TR level structure of the spin isomers of H_2 and H_2O inside C_{60} even sparser.

The quantum TR dynamics of light-molecule endofullerenes has attracted considerable interest from experimentalists and theorists alike within the past decade. The fullerene cages, that of C_{60} in particular, have emerged as remarkable nanolaboratories[16] in which the endohedral molecules are to a large extent, although not completely, isolated from the external environment beyond the host cage. In addition, the intermolecular TR motions of the endohedral molecule couple very weakly to both its intramolecular vibration(s) and those of the fullerene (allowing both monomers to be treated as rigid to a very good approximation). These simplifying features have greatly facilitated comprehensive spectroscopic studies of their highly quantum behavior in nanoconfinement. They have also made it possible for theory to provide detailed understanding of the quantum TR dynamics at a fundamental level, describe it quantitatively from first principles and, through direct comparison with experiments, play the key role in their interpretation and analysis.

$H_2@C_{60}$ was the first light-molecule endofullerene to be synthesized,[6,7] and is paradigmatic in many ways. Not surprisingly, the quantum TR dynamics of H_2 and its isotopologues caged in C_{60} has been the subject of by far the largest number of theoretical[13,17–22] and experimental studies, primarily inelastic neutron scattering (INS)[23–26] and infrared (IR).[19,27–29] Its key features were first elucidated in a series of theoretical investigations.[13,17–20] They revealed that the purely translational eigenstates can be assigned with the quantum numbers of the 3D isotropic harmonic oscillator (HO), the principal quantum number $n = 0,1,2,\ldots$, and the orbital angular momentum quantum number $l = n, n-2, \ldots, 1$ or 0, for odd and even n, respectively. The rotational energy levels of the caged H_2 can be assigned in terms of the quantum numbers $j = 0,1,2,\ldots$, of a linear rigid rotor. An unanticipated finding that emerged from these theoretical studies was that the TR states of $H_2@C_{60}$ with simultaneous translational and rotational excitation display vectorial coupling between the orbital angular momentum **l** associated with the translational c.m. motion of H_2 and the rotational angular momentum **j** to give the total angular momentum with the quantum numbers $\lambda = l + j, l + j - 1, \ldots, |l - j|$, and the degeneracy of $2\lambda + 1$.[13] The fingerprints of this coupling are the splittings of such TR eigenstates into as many closely spaced levels as there are values of λ, each having the degeneracy $2\lambda + 1$.[13,17]

It turned out that the TR energy level structure of $H_2O@C_{60}$, determined by means of rigorous quantum 6D calculations,[14] exhibits all the qualitative features above of $H_2@C_{60}$. These include the coupling of the orbital and rotational angular momenta and the use of 3D HO quantum numbers n and l to assign the translational excitations, while for the H_2O rotational excitations the asymmetric top quantum numbers $j_{k_a k_c}$ are used. The TR eigenstates of $HF@C_{60}$ from the recent quantum 5D calculations[30] were also assigned in terms of the quantum numbers (n, l, j, λ) utilized for $H_2@C_{60}$[13,17] and $HD@C_{60}$.[17] Thus, a unified theoretical picture exists of the quantum TR dynamics of the three light-molecule endofullerenes $M@C_{60}$ (M = H_2, H_2O, HF).

A major step forward in the ability of theory to provide a reliable interpretation and assignment of the INS spectra of light-molecule endofullerenes was the development of the methodology for rigorous quantum calculation of the INS spectra of a hydrogen molecule, and diatomic molecules in general, inside a nanocavity.[31–33] This methodology, that incorporates the computed quantum 5D TR eigenstates, has been employed for the highly realistic quantum simulations of the INS spectra of H_2 and HD in C_{60}.[21,22,34] These simulations have led to the entirely surprising discovery of a selection rule in the INS spectroscopy of H_2[22] and HD[21] confined inside near-spherical nanocavities such as that of C_{60}. This selection rule was the first ever to be established for the INS spectroscopy of discrete molecular compounds. Shortly thereafter, it was confirmed experimentally[34] and generalized.[35,36]

An assumption made in all of the above studies of $H_2@C_{60}$,

This journal is © The Royal Society of Chemistry [year]

theoretical and experimental, was that the cage encapsulating the guest H_2 has I_h symmetry, which is that of an isolated C_{60} molecule. If the confining environment has this symmetry, then the $j = 1$ ground state of *ortho*-H_2 would remain three-fold degenerate, as in the gas phase. And indeed, in the INS spectra of $H_2@C_{60}$,[23–26] the peak associated with the transition between the ground states of *para*- and *ortho*-H_2 showed no evidence of splitting to within the resolution of the measurements. But, starting in 2009, two investigations of solid $H_2@C_{60}$ employing more sensitive experimental approaches yielded a different result. First, from the specific heat anomaly observed at low temperatures (below 4 K) for $H_2@C_{60}$, Kohama *et al.*[37] inferred that the $j = 1$ triplet of *ortho*-H_2 is in fact split, by about 1.13 cm^{-1}, into a lower-energy state that is non-degenerate and a doubly degenerate higher-energy state. The implication of this observation was that the symmetry of the environment felt by the guest H_2 must be lower than I_h.

The symmetry breaking in $H_2@C_{60}$ has been detected by the INS spectroscopy as well,[38] but only indirectly, by carefully investigating the temperature dependence of the line (its shape, width, and peak position) corresponding to the transitions from the ground state of *ortho*-H_2 to the ground state of *para*-H_2 (neutron energy gain), in the range 0.06-35 K. From a multi-component analysis of the data it was deduced that the $j = 1$ triplet of *ortho*-H_2 is split into a lower-energy level that is non-degenerate and a higher-energy doubly degenerate level, separated by 1.09 cm^{-1}. This result is very close to the splitting of 1.13 cm^{-1} obtained by Kohama *et al.*[37]

In neither of these studies[37,38] was the splitting of the ground state of *para*-H_2 observed directly. However, the low-temperature (6 K) near-IR absorption spectra of solid $H_2@C_{60}$[19,29] exhibit a set of Q(1) transitions originating in the ground state of *ortho*-H_2 to three $n = 1, j = 1$ sublevels corresponding to $\lambda = 1, 2, 0$, respectively, in the order of increasing energies. One of them, the $\lambda = 0$ band, is clearly split by about 1 cm^{-1}. This splitting was noted and commented only briefly, mentioning the possibility of the distortion of the C_{60} cage due to unspecified causes. Although its value was very similar to the splitting measured by Kohama *et al.*,[37] no connection to this result was made in these papers.[19,29] The simulations of the near-IR spectra of solid $H_2@C_{60}$ presented in this paper demonstrate rather conclusively that this spectroscopic feature can be indeed attributed to, and its magnitude reflects, the splitting of the initial state of the transition, the *ortho*-H_2 $j = 1$ ground state.

Experimental observations of the splitting of the $j = 1$ level of the guest molecule in C_{60} have not been limited to H_2. Clear and direct evidence of symmetry breaking has been found for $H_2O@C_{60}$ and $HF@C_{60}$, where both guest molecules have permanent electric dipoles. The early INS and nuclear magnetic resonance (NMR) spectra of solid $H_2O@C_{60}$[39] showed that the three-fold degenerate 1_{01} ground state of *ortho*-H_2O was split by about 4.8 cm^{-1} into a non-degenerate lower-energy state and a doubly degenerate higher-energy state. The subsequent more detailed INS investigation using a highly purified sample of $H_2O@C_{60}$ confirmed this splitting pattern, and yielded the splitting of 4.19 cm^{-1} .[40] For $HF@C_{60}$, the symmetry breaking manifested in the far- and mid-IR spectra of the polycrystalline sample[9] (measured at 5 K) as the 3.9 cm^{-1} splitting of the $j = 0 \rightarrow j = 1$ transition.

The fact that experiments have revealed the splitting of the three-fold degenerate ground states of *ortho*-H_2, *ortho*-H_2O, and the $j = 1$ state of HF, when these molecules are inside C_{60}, in solid C_{60} and at low temperatures, strongly suggested that the symmetry breaking was not accidental but an inherent feature of such systems. It was also clear that having a permanent electric dipole was not a prerequisite, since symmetry breaking was present regardless of whether the endohedral molecule has a permanent electric dipole (H_2O, HF) or not (H_2). But, the origin, or mechanism responsible for the symmetry breaking remained uncertain. A couple of possibilities have been proposed: the distortion of the host C_{60} cage due to the interaction with the guest molecule in its interior,[9,38–40] and, when the guest molecules have a permanent electric dipole (H_2O, HF), dipolar interactions between the guest molecules in neighboring C_{60} cages, possibly resulting in the alignment of their dipoles thus breaking the symmetry of the solid.[39,40] However, no quantitative predictions have been made based on these mechanisms, precluding the possibility of testing their validity by comparison with the measured splittings.

Motivated by this unsatisfactory state of affairs, very recently,[41] in order to gain a quantitative understanding of the symmetry breaking in light-molecule endofullerenes $M@C_{60}$ (M = H_2, H_2O, HF), we developed a model, that proved highly successful, based on the following considerations. At temperatures below 90 K, the rotations of the fullerene molecules in the solid C_{60} are entirely frozen,[42] and the crystal structure is simple cubic (sc, $Pa\bar{3}$). The C_{60} molecules are locked in, and coexist as, two orientationally ordered configurations of neighboring units. The dominant one, referred to as the P orientation, corresponds to the global minimum of the inter-cage potential, and has the electron-rich double bonds shared by two hexagons (denoted 6:6) of one C_{60} unit facing directly the electron-poor pentagons of the neighboring cages.[42,43] Each C_{60} unit has six electron-rich 6:6 bonds and six electron-deficient pentagons facing its twelve nearest neighbors. In the slightly higher local minimum on the inter-cage potential, the C_{60} molecules have the H orientation, where electron-rich 6:6 bonds of one C_{60} are immediately adjacent to the electron-poor hexagonal faces of the neighboring units.[42] Below 90 K and at ambient pressure, the relative proportion of molecules in the P and H orientations is 5:1.[42] The relevance of the P and H orientations for symmetry breaking is that in both orientations the point-group symmetry of the environment at the center of a C_{60} cage is S_6,[37,38] that in principle can cause the splitting of the three-fold degeneracy of the ground states of *ortho*-H_2, *ortho*-H_2O, and the $j = 1$ state of HF into a non-degenerate and a doubly degenerate state, as observed experimentally. However, for the consequences of this symmetry lowering to be observable, the guest molecule inside one C_{60} must have appreciable interaction not with just its own host cage (whose symmetry is presumably still I_h), but also with the neighboring C_{60} units. It is this latter interaction that leads to the symmetry breaking, but its nature has been unresolved.

In the recent paper,[41] we have identifed the origin of this crucial interaction in the endofullerenes $M@C_{60}(s)$ (M = H_2, HF,

H_2O), and verified it by direct comparison of its predictions with the experimental results. This was achieved by developing a model that considers a fragment of solid C_{60} comprised of twelve nearest-neighbor (NN) cages around the central cage, with all the cages being in either the P or the H orientation. The cages are treated as rigid, and assumed to have I_h symmetry. Only the central cage is occupied by the guest molecule M, while the twelve NN cages are left empty. The key proposition of the model is that the predominant source of the symmetry breaking in M@$C_{60}(s)$ at low temperatures is the electrostatic interaction between the charge densities on the NN C_{60} cages and that on M, and moreover, that retaining just its leading quadrupole terms suffices to quantitatively account for the manifestations considered in this study. The symmetry of the environment felt by M in the central C_{60} cage generated by this electrostatic interaction with the NN cages of the fragment is S_6. The electron density on the NN cages was obtained from a first-principles DFT calculation, and the charge density on M is related to its body-fixed (BF) quadrupole moments reported in the literature. Thus, the M-NN electrostatic interaction contains no adjustable parameters.

The splittings of the ground states of *ortho*-H_2, *ortho*-H_2O and the $j = 1$ level of HF inside the central C_{60} and under the quadrupolar interaction with the twelve NN cages have been computed for the P and H orientations by means of variational calculations in 5D (H_2) and 6D (H_2O), as well as by the first-order perturbation theory (H_2, HF, and H_2O). The two methods yielded very similar results.[41] For the P orientation, the calculated splittings agree extremely well, to within the experimental error bars, with those measured for the corresponding M@$C_{60}(s)$ systems. In addition, the calculations yield the 1:2 splitting patterns in agreement with the experiments. This quantitative success of the model lends strong support to its central assumption, that the low-temperature symmetry breaking in the M@$C_{60}(s)$ species considered arises primarily from the M-NN interaction, dominated by the leading quadrupole terms. Additional support for this model is provided by the fact that the splittings of the levels considered, calculated and experimental, scale linearly with the magnitudes of the quadrupole moments of the endohedral molecules. A most surprising result of these calculations was that the symmetry-induced splittings obtained for the H orientation are about a factor of 30 smaller than the corresponding ones in the P orientation, for the three endofullerene systems considered.[41]

In this paper, our investigation extends beyond the symmetry breaking of the ground states of *ortho*-H_2, *ortho*-H_2O and the $j = 1$ level of HF inside C_{60} studied earlier.[41] We report the TR eigenstates of the endofullerenes M@C_{60} (M = H_2, H_2O, HF), calculated variationally for the 13-C_{60} fragment of crystalline $C_{60}(s)$ and the quadrupolar M-NN interaction defined previously,[41] for both the P and H crystal orientations. As before, the cages are taken to be rigid, and assumed to have I_h symmetry. Only the central cage is occupied by M. The effects of symmetry breaking on the excited TR levels of M in the central C_{60} cage of the fragment are investigated, and for the P orientation the level splittings are found to vary drastically with the nature of the excitation, rotational or translational, involved. In addition, using the TR eigenstates computed in this work, for M = H_2 we simulate the low-temperature near-IR (NIR) spectra involving the combination bands built off the intramolecular vibrational fundamental, while for M = HF and H_2O, low-temperature far-IR (FIR) spectra consisting of direct transitions between TR eigenstates are simulated. For each of the species, both the FIR and NIR spectra are simulated for the P and H orientations separately, and presented also as the appropriately weighted sums (0.15H + 0.85P). In all instances, the simulated weighted-sum spectra are in excellent agreement with the available experimental spectra.

The paper is organized as follows. In Section 2, the theory for calculating the TR eigenstates of endohedral molecules inside the cages of $C_{60}(s)$ is presented, together with our approach to the eigenfunction analysis. The methodology for the simulation of the NIR and FIR spectra of the caged molecules, utilizing the computed TR eigenstates, is also described in this section. Theoretical results, TR eigenstates and the simulated spectra, are presented and discussed in Section 3. Conclusions are given in Section 4.

2 Theory

2.1 Hamiltonian

We have previously reported[41] on the details of our approach toward modeling the hindered TR states of endohedral fullerenes of the form M@C_{60} when such are embedded in the lattice of crystalline $C_{60}(s)$. As noted in Section 1 we assume that these states largely derive from the interaction of M with the central C_{60} cage within which it resides, but that they are also influenced by the electrostatic interaction between M and the twelve NN cages in the lattice. In particular, we take the TR Hamiltonian to be given by

$$\hat{H} = \hat{T} + V_{\mathrm{M-C_{60}}} + V_{\mathrm{ES}}, \tag{1}$$

where $\hat{T}$ is the operator associated with the TR kinetic-energy of M, $V_{\mathrm{M-C_{60}}}$ is that part of the potential energy surface (PES) arising from the M-central cage interaction, and V_{ES} is that part of the PES due to the M-NN interaction. It is the latter term that gives rise to the breaking of the icosahedral symmetry of the species. Both M and C_{60} monomers are taken to be rigid.

The $V_{\mathrm{M-C_{60}}}$ functions that we use are PESs available from the literature. The empirically-derived, pairwise-additive five-dimensional (5D) PES from Xu *et al.*[22] is used for M = H_2 for the TR manifold associated with the ground state of the intramolecular vibrational mode ($v = 0$) and that from Xu *et al.*[18] is used for the $v = 1$ manifold. For M = HF we employ the surface produced by Kalugina and Roy[30] from the fitting of *ab initio*-computed interaction energies to a bipolar spherical-tensor expansion. The M = H_2O 6D potential function employed is the pairwise-additive function adapted to H_2O@C_{60} by Felker and Bačić[14] from the "MD1" graphene-water PES produced by Farimani *et al.*[44] Details pertaining to $\hat{T}$ and $V_{\mathrm{M-C_{60}}}$ for all three species are given in the ESI.† We note that the C_{60} geometry that we assume here (from Felker *et al.*[41]) is slightly different than the ones used elsewhere in M = H_2[18,22] and M = H_2O[14] studies. In consequence, the TR eigenstates computed here for isolated M@C_{60} (no NN interaction) differ slightly from the ones computed in those works.

For V_{ES} we retain only the leading term in the multipole expan-

This journal is © The Royal Society of Chemistry [year]

sion of the M-NN interaction.[41] Given the S_6 point-group symmetry of the 13-cage (central + NN) crystal fragment,[45,46] that term is the quadrupolar one:

$$V_{\rm ES} \simeq V_{\rm quad} = \sum_{m=-2}^{2} (-1)^m Q_m^{(2)} I_{-m}^{(2)}, \qquad (2)$$

where the $Q_m^{(2)}$ constitute the electric-quadrupole spherical tensor of M@C_{60} and the $I_m^{(2)}$ constitute the electric-field-gradient tensor arising from the charges on the NN cages.

The M@C_{60} quadrupole tensor can be written in terms of the TR coordinates of M.[41] That is, (*i*) the spherical coordinates $\mathbf{R} = (R,\Theta,\Phi)$ that describe the position of the c.m. of M relative to a space-fixed (SF) Cartesian axis system affixed to the central cage, and (*ii*) the Euler angles (ω) that describe the orientation, relative to the SF axes, of BF axes affixed to M:

$$\begin{aligned} Q_m^{(2)}(\mathbf{R},\omega) &= \left[\sum_{q=-2}^{2} [D_{m,q}^{(2)}(\omega)]^* Q_q^{\rm BF}\right] \\ &+ \left[\sqrt{40\pi}\mu R \sum_{m',m''=-1}^{1} (-)^m \begin{pmatrix} 1 & 1 & 2 \\ m' & m'' & -m \end{pmatrix}\right. \\ &\times \left. Y_{1,m'}(\Theta,\Phi)[D_{m'',0}^{(1)}(\omega)]^*\right], \end{aligned} \qquad (3)$$

where $Q_q^{\rm BF}$ is the permanent quadrupole tensor of M in the body-fixed frame and $\mu\hat{z} = \vec{\mu}$ is the permanent electric dipole of M, taken to lie along the BF $\hat{z}$ axis. The values for $Q_q^{\rm BF}$ and μ that we have used for each species are given in the ESI.†

The electric-field-gradient tensor can be determined from the charge-density function of an individual C_{60} and from the geometry of the NN cages about the central cage. We have computed[41] the former by using density functional theory. The latter is available from the literature for the P and the H orientations.[42] Together, these yield[41] for the case (adopted herein) in which the C_3 symmetry axis of the 13-cage fragment points along the (1,1,1) direction in the SF frame:

$$[I_m^{(2)}] = A(i,-1+i,0,1+i,-i); \qquad m = -2,-1,0,+1,+2 \qquad (4)$$

where $A = 6.809\times10^{-6}$ a.u. for the P orientation and $A = -2.307\times10^{-7}$ a.u. for the H orientation.

2.2 Diagonalization of $\hat{H}$

We use the Chebyshev version[47] of filter diagonalization[48] (CFD) to compute the low-energy TR eigenstates of $\hat{H}$ variationally. The implementation of CFD involves the repeated multiplication of a random initial state vector $|\psi\rangle$, expressed in some primitive basis, by the matrix of $\hat{H}$, expressed in the same basis. The primitive bases that we employ consist of states, each of which is a product of a 3D isotropic HO (3D-HO) eigenstate covering the **R** degrees of freedom and a rigid-rotor eigenstate covering the ω degrees of freedom.

The 3D-HO states are of the form $|n,l,m_l\rangle$, where the principal quantum number $n = 0,1,2,\ldots,n_{\rm max}$, the orbital angular momentum quantum number $l = n,n-2,\ldots \geq 0$, and the azimuthal angular momentum quantum $m_l = -l,-l+1,\ldots,l$. In any given basis the eigenfunctions associated with these states[41] depend on the choice of the value for a parameter $\beta = 2\pi M\nu$, where M is the mass of the oscillator and ν is its linear frequency. We have used $\beta = 2.989$ au, 12.0 au, and 24.38 au for H_2@C_{60}, HF@C_{60}, and H_2O@C_{60}, respectively. These values correspond to c.m. hindered-translational modes having frequencies of about 180 cm^{-1}, 72.3 cm^{-1}, and 163.2 cm^{-1}, respectively, for these species.

The rigid-rotor states for M = H_2 and M = HF are the usual, linear rigid-rotor states $|j,m_j\rangle$, with $j = 0,1,\ldots,j_{\rm max}$ and $m_j = -j,-j+1,\ldots,j$. Their functional representations are spherical harmonics $Y_{j,m_j}(\omega)$. The rotational states for M = H_2O are symmetric-top eigenfunctions of the form $|j,m_j,k\rangle$, with $j = 0,1,\ldots,j_{\rm max}$, $m_j = -j,-j+1,\ldots,j$, and $k = -j,-j+1,\ldots,j$. Their functional representations are normalized Wigner rotation matrix elements $\sqrt{2j+1/8\pi^2}[D_{m_j,k}^{(j)}(\omega)]^*$. The values that we use for $n_{\rm max}$ are 8, 10 and 8 for H_2, HF, and H_2O, respectively, and $j_{\rm max} = 8$ for all three. In the case of both M = H_2 and M = H_2O, the matrix of $\hat{H}$ can be rigorously block diagonalized into *para* and *ortho* blocks. For M = H_2 (H_2O) the *para* basis states correspond to even j (k) and the *ortho* ones to odd j (k).

The matrix elements of $\hat{T}$ in each of the 3D-HO/rigid-rotor bases can be computed analytically. Hence the effect of multiplying a given state vector by that matrix is straightforward in each case. Analogous multiplication by the full (i.e., $V_{\rm M-C_{60}} + V_{\rm quad}$) potential-energy matrix was accomplished by (*i*) transforming the state vector to a grid representation, (*ii*) multiplication of the transformed vector at each grid point by the value of the potential at that point, and (*iii*) transformation of the result back to the basis representation. The general nature of the 5D grids employed for M = H_2 and HF and that of the 6D grid employed for M = H_2O are described in Felker *et al.*,[41] Section 2.5. The grid parameters specific to the calculations reported here are given in the ESI.†

2.3 Eigenfunction analysis

As mentioned in Section 1, the close-to-isotropic S_6 environment experienced by M inside a C_{60} in $C_{60}(s)$ renders several quantum numbers associated with the TR eigenstates (at least the low-energy ones) "almost good." In characterizing a given eigenstate it is thus relevant to enumerate the values that such quantum numbers take on for that state, and to have a measure as to their degree of goodness.

The best two (typically) of these quantum numbers are the ones associated with the combined orbital and rotational angular momenta of M. λ is one of these, and $|m_\lambda|$ is the other. The latter is the absolute value of the component of λ along the C_3 axis (i.e., Z') of the S_6 point group. In our presentation of results below we give a measure of the value of λ for each state by computing the expectation value $\langle|\mathbf{l}+\mathbf{j}|^2\rangle$ and solving for the value $\langle\lambda\rangle$ that satisfies $\langle\lambda\rangle(\langle\lambda\rangle+1) = \langle|\mathbf{l}+\mathbf{j}|^2\rangle$. The degree to which this value is close to an integer reflects how close the state is to being an eigenstate of $|\mathbf{l}+\mathbf{j}|^2$. We also quote the value of $|m_\lambda|$ that con-

tributes most to each state along with the total contribution that basis states having that value contribute to the eigenstate.

The quantum numbers n,l,j are also close-to-good for the low-energy states of the three species (particularly for M = H_2 and M = H_2O). For each of the eigenstates ($|I\rangle$) of M = H_2 and M = HF we have computed the quantities

$$P_I(n,l,j) \equiv \sum_{m_l,m_j} |\langle n,l,m_l,j,m_j|I\rangle|^2 \tag{5}$$

for all (n,l,j). In presenting results we list the set of these quantum numbers that contributes most to $|I\rangle$, along with the associated $P_I(n,l,j)$ value. For $H_2O@C_{60}$ we compute instead the quantities

$$P_I(n,l,j_{k_ak_c}) \equiv \sum_{m_l,m_j} |\langle n,l,m_l,j_{k_ak_c},m_j|I\rangle|^2 \tag{6}$$

where the $|j_{k_ak_c},m_j\rangle$ are the (asymmetric-top) rotational eigenfunctions of free H_2O in its ground vibronic state. In presenting the M = H_2O results we list the major $(n,l,j_{k_ak_c})$ contributor to each $|I\rangle$ together with the associated $P_I(n,l,j_{k_ak_c})$ value.

2.4 Simulations of far-infrared and near-infrared spectra

We have noted in Section 1 that IR absorption spectroscopies in the far-IR (FIR) and near-IR (NIR) are two of the means by which the symmetry breaking in $M@C_{60}(s)$ samples has been proven.[9,19,29] Given this, the electrostatic model can be tested, in principle, by comparing experimental spectra with simulations based on the eigenstates of $\hat{H}$ that we compute here. We have performed such simulations for all three species. For M = HF and M = H_2O we simulate FIR spectra consisting of direct transitions between TR eigenstates. For M = H_2 we simulate NIR spectra consisting of combination bands built off the H_2 intramolecular vibrational fundamental. In each of these cases we first compute the relative transition strengths between the set of initial states $|i\rangle$ and final states $|f\rangle$ as

$$S_{fi}(\omega_{fi}) = \mathrm{Pop}_i \omega_{fi} \sum_{q=-1}^{1} |\langle f|\mu_q|i\rangle|^2, \tag{7}$$

where Pop_i is the relative thermal population of state $|i\rangle$, $\omega_{fi} = E_f - E_i$ is the energy difference between the states, and the μ_q are the components of the spherical-vector representation of the electric-dipole operator in the SF frame. This orientationally averaged form for S_{fi} is appropriate given that the samples on which the experiments have been performed are powder-crystalline ones.[9,19,29] We then compute the spectrum as

$$I(\omega) = \sum_{i,f} \int_{-\infty}^{\infty} G(\omega-\omega_{fi}) S_{fi}(\omega_{fi}) d\omega, \tag{8}$$

where $G(\omega)$ is a Gaussian instrument-response function with a predetermined resolution defined by a full-width at half-maximium (FWHM).

2.4.1 FIR spectra

For the FIR spectra we take the electric dipole to be the permanent dipole of the relevant molecule. With our choice of primitive bases and of the direction of the dipoles in the BF frame (i.e., $\vec{\mu} = \mu\hat{z}$) this leads straightforwardly to expressions for the dipole matrix elements for M = HF:

$$\begin{aligned}\langle f|\mu_q|i\rangle &= \mu \sum_{n,l,m_l} \sum_{j,j'} \sum_{m_j,m'_j} \langle f|n,l,m_l,j',m'_j\rangle\langle n,l,m_l,j,m_j|i\rangle \\ &\times (-1)^{m'_j}\sqrt{\bar{j}'\bar{j}} \begin{pmatrix} j' & 1 & j \\ 0 & 0 & 0 \end{pmatrix} \begin{pmatrix} j' & 1 & j \\ -m'_j & q & m_j \end{pmatrix},\end{aligned} \tag{9}$$

where $\bar{j} \equiv (2j+1)$. For M = H_2O:

$$\begin{aligned}\langle f|\mu_q|i\rangle &= \mu \sum_{n,l,m_l} \sum_{j,j',k} \sum_{m_j,m'_j} \langle f|n,l,m_l,j',m'_j,k\rangle\langle n,l,m_l,j,m_j,k|i\rangle \\ &\times (-1)^{m'_j+k}\sqrt{\bar{j}'\bar{j}} \begin{pmatrix} j' & 1 & j \\ -k & 0 & k \end{pmatrix} \begin{pmatrix} j' & 1 & j \\ -m'_j & q & m_j \end{pmatrix}.\end{aligned} \tag{10}$$

2.4.2 NIR spectra

For the NIR $v = 0 \rightarrow 1$ spectra of $H_2@C_{60}$ we follow Mamone *et al.*[19] In that work the dipole induced on the H_2 moiety by the constraining environment is expanded in terms of bipolar spherical tensors – $F^{1,J}_{1,q}(\Omega)$ – that depend on the angles $\Omega \equiv (\Theta,\Phi,\omega)$. The matrix elements of the μ_q can then be straightforwardly evaluated if the $H_2@C_{60}$ TR states in the $v=0$ and $v=1$ manifolds are eigenstates of $|\mathbf{l}+\mathbf{j}|^2$, $\mathbf{l}^2$, $\mathbf{j}^2$, and $(l+j)_{Z'}$. In particular, adapting eqn (6) of Mamone, *et al.*[19]

$$\langle f|\mu_q|i\rangle = \frac{4\pi}{\sqrt{3}} \sum_{J=0,2} \rho^J \langle F^{l_f,j_f}_{\lambda_f,m_{\lambda,f}}(\Omega)|F^{1,J}_{1,q}(\Omega)|F^{l_i,j_i}_{\lambda_i,m_{\lambda,i}}(\Omega)\rangle, \tag{11}$$

where the radial factors, ρ^J, are determined from experiment to be in the ratio $\rho^0/\rho^2 = -2.0$, and the angular factors are given by the Wigner-Eckart theorem as

$$\begin{aligned}\langle F^{l_f,j_f}_{\lambda_f,m_{\lambda,f}}|F^{1,J}_{1,q}|F^{l_i,j_i}_{\lambda_i,m_{\lambda,i}}\rangle &= (-1)^{\lambda_f+m_{\lambda,f}} \begin{pmatrix} \lambda_f & \lambda_i & 1 \\ -m_{\lambda,f} & m_{\lambda,i} & q \end{pmatrix} \\ &\times \langle l_f,j_f,\lambda_f||F^{1,J}_{1,q}||l_i,j_i,\lambda_i\rangle,\end{aligned} \tag{12}$$

with

$$\begin{aligned}\langle l_f,j_f,\lambda_f||F^{1,J}_{1,q}||l_i,j_i,\lambda_i\rangle &= (-1)^{l_f+j_f}\frac{3}{4\pi}\sqrt{\bar{\lambda}_f\bar{\lambda}_i\bar{l}_f\bar{l}_i\bar{j}_f\bar{j}_i\bar{J}} \\ &\times \begin{pmatrix} l_f & 1 & l_i \\ 0 & 0 & 0 \end{pmatrix} \begin{pmatrix} j_f & J & j_i \\ 0 & 0 & 0 \end{pmatrix} \begin{Bmatrix} l_f & l_i & 1 \\ j_f & j_i & J \\ \lambda_f & \lambda_i & 1 \end{Bmatrix},\end{aligned} \tag{13}$$

and $\bar{\lambda} \equiv (2\lambda+1)$, $\bar{l} \equiv (2l+1)$, etc.

In order to employ eqn (11) here we use the results of our eigenfunction analysis to assign λ, m_λ, l and j values to the relevant TR states. This is an approximation, but a very good one for the low-energy $H_2@C_{60}$ TR states involved.

This journal is © The Royal Society of Chemistry [year]

3 Results and discussion

Tables 1 to 3 present results of the TR eigenstate calculations for M = H_2, HF, and H_2O, respectively, for the P crystal orientation. In the Tables we give for each level its energy relative to the TR ground state (ΔE_P), its degeneracy (g_P), and the results from the eigenfunction analysis outlined in Subsection 2.3. We group together those levels whose parentage derives from the same level of the isolated M@C_{60} molecule. The energies (ΔE_0) and degeneracies (g_0) of these "parent" levels are also given in the first two columns of the Tables so that the quadrupole-induced splittings of the latter can be readily ascertained. Finally, for the M = H_2 species we give in parentheses in column 3 the computed energies, relative to the $v = 1$ TR ground state, of the $v = 1$ TR levels that participate as final states in that portion of the $v = 0 \rightarrow 1$ NIR spectrum that we have simulated for $H_2@C_{60}(s)$.

In addition to P-orientation calculations we have also computed the low-energy TR states for each of the three species for the H crystal orientation. The calculated quadrupole-induced splittings for all the states of these species are less than 0.1 cm^{-1}. We do not enumerate those results in detail here because they are so close to those of the corresponding isolated M@C_{60}. The small splittings for the H orientation relative to those for the P are due, of course, to the order-of-magnitude smaller electric-field-gradient moments for the former.[41]

Going back to the P-orientation results of Tables 1 to 3, several points are of note. First, as reported in Felker *et al.*,[41] the computed splittings for the *ortho* ground states in M = H_2 ($|n,l,j\rangle = |0,0,1\rangle$) and in M = H_2O ($|n,l,j_{k_pk_o}\rangle = |0,0,1_{01}\rangle$) and that for the $|n,l,j\rangle = |0,0,1\rangle$ level of M = HF (1.09 cm^{-1}, 4.22 cm^{-1}, and 3.72 cm^{-1}, respectively) all match the splittings measured for these levels, as well as the measured 1:2 degeneracy ordering of the split states. That is, our $j = 1$ results are consistent with all of the extant experimental results on symmetry-breaking in these species.[9,19,29,37–40]

Second, the computed splittings for numerous other *rotationally excited* levels in each of the species have magnitudes similar to those for the $j = 1$ levels. However, and in contrast, the splittings for levels that are pure *translational* excitations are about an order of magnitude smaller than the former. This is true for all three species. Thus, the splittings of the $|1,1,0\rangle$ levels in M = H_2, HF, and H_2O are only 0.04 cm^{-1}, 0.18 cm^{-1} and 0.41 cm^{-1}, respectively. Similarly small splitting magnitudes characterize the $n = 2, j = 0$ levels in the species. This dichotomy between the splitting of excited levels that have some rotational excitation and ones that do not is readily understood in the context of the electrostatic/quadrupole model. The matrix elements of the quadrupole operator $Q_m^{(2)}$ (see eqn (3)) between $j = 0$ states are identically zero. This is not true, however, for $j \neq 0$ states. Hence, the degenerate first-order couplings that produce, for example, the large splittings of the $|0,0,1\rangle$ levels in each of the three species, are not possible between states of the $|1,1,0\rangle$ level. It is important to note that other symmetry-breaking mechanisms - e.g., central cage distortion - will not necessarily give rise to this same translation/rotation splitting dichotomy.

Third, we note that the total angular momentum quantum number λ is close to an integer for the TR eigenstates of the three species shown in Tables 1 to 3, with but a few exceptions, and so is $|m_\lambda|$. Hence, both λ and $|m_\lambda|$ largely remain very good quantum numbers in the presence of the quadrupolar M-NN interaction, and can be used to label the TR eigenstates.

The situation is somewhat different with respect to the quantum numbers n,l,j for M = H_2 and HF, and $n,l,j_{k_ak_c}$ for M = H_2O, in Tables 1 to 3. In the case of M = H_2 and H_2O, these quantum numbers are very good, in the sense that for H_2 the lower-energy TR eigenstates have $P_l(n,l,j)$ values very close to 1, and for H_2O, $P_l(n,l,j_{k_ak_c})$ is almost always greater than 0.8 or 0.9. In contrast, for M = HF, apart from the few lowest eigenstates, $P_l(n,l,j)$ is typically in the range 0.5-0.6, implying that n,l,j are not nearly as good quantum numbers for HF as they are for H_2. We attribute this difference to the fact that HF exhibits large mass asymmetry, unlike the homonuclear H_2. A similar situation was encountered in an earlier study of the quantum TR dynamics of H_2, HD, and D_2 in C_{60},[17] where j was found to be a very good quantum number for the homonuclear isotopologues H_2 and D_2, but much less so for the heteronuclear HD. Such mass asymmetry shifts the position of M's c.m. at the minimum of the PES from the center of the C_{60} cage to a nonzero R value. This, in turn, gives rise to enhanced translation-rotation coupling for the species with mass asymmetry. While H_2O also exhibits substantial mass asymmetry, this coupling is particularly effective for HF owing to the fact that its translational fundamental is much closer in energy to the lowest-lying rotational excitation of the species than in the case of H_2O.

Let us turn now to the results of the NIR and FIR simulations. We start with the NIR simulations of $H_2@C_{60}(s)$ spectroscopy. These pertain to the one *para* $Q(0)$ band and the three *ortho* $Q(1)$ bands associated with the transitions originating in the $v = 0$ *para* and *ortho* TR ground-state levels (i.e., $|n,l,j,\lambda''\rangle = |0,0,0,0\rangle$ and $|0,0,1,1\rangle$, respectively) and ending in the $v = 1$ *para* $|1,1,0,1\rangle$ and *ortho* $|1,1,1,\lambda'\rangle$, $\lambda' = 0,1,2$ levels, respectively. It is the observed splitting on the $Q(1)$, $\lambda' = 0$, band[19,29] that is one of the pieces of evidence for symmetry-breaking in the species. Figure 1 shows results from our simulations. The lower trace in the figure gives the *ortho* spectrum (red) and the *para* spectrum (blue) for the H orientation at high resolution (0.1 cm^{-1}). The middle trace shows analogous spectra for the P orientation.

Finally, the upper spectrum is the weighted sum of spectra 0.15H + 0.85P (corresponding to the measured abundances of the two crystal types under the experimental conditions) at a resolution of 0.7 cm^{-1}. In all of these spectra the $v = 0$ *ortho/para* population ratio was taken to be 3:1 and the relative populations of the *ortho* states were taken to conform to a 6-Kelvin Boltzmann distribution. From the spectra, one sees that the quadrupole-induced splittings of all three of the $Q(1)$ bands are appreciable for the P crystal orientation and would be observable at 0.1 cm^{-1} resolution. However, at the lower resolution more in line with experiment, and with the contribution from the H-orientation included, only the splitting of the $Q(1)$, $\lambda' = 0$ band is apparent, consistent with experiment. Thus, the electrostatic model predicts not only the $j = 1$ splitting magnitude, it is also reproduces the qualitative features of the NIR spectrum.

Table 1 Properties of computed TR eigenstates for $H_2@C_{60}$

$\Delta E_0/\mathrm{cm}^{-1}$	g_0	$\Delta E_P/\mathrm{cm}^{-1}$	g_P	(n,l,j)	$P_I(n,l,j)$	$\langle\lambda\rangle$	$\lvert m_\lambda\rvert$	$P_I(\lvert m_\lambda\rvert)$
para:								
0.00	1	0.00	1	(0, 0, 0)	0.9979	0.000	0	1.0000
186.71	3	186.70 (191.65)	2	(1, 1, 0)	0.9867	1.000	1	1.0000
		186.74 (191.69)	1	(1, 1, 0)	0.9868	1.000	0	1.0000
349.80	5	349.29	1	(0, 0, 2)	0.9861	2.000	0	1.0000
		349.54	2	(0, 0, 2)	0.9860	2.000	1	1.0000
		350.32	2	(0, 0, 2)	0.9855	2.000	2	1.0000
389.43	5	389.42	2	(2, 2, 0)	0.9492	2.000	2	0.9996
		389.44	2	(2, 2, 0)	0.9497	2.000	1	0.9998
		389.45	1	(2, 2, 0)	0.9499	2.000	0	0.9999
ortho:								
116.73	3	116.00	1	(0, 0, 1)	0.9977	1.000	0	1.0000
		117.09	2	(0, 0, 1)	0.9977	1.000	1	1.0000
298.22	3	297.99 (295.49)	2	(1, 1, 1)	0.9891	1.010	1	1.0000
		298.59 (296.08)	1	(1, 1, 1)	0.9891	1.000	0	1.0000
304.53	5	304.14 (302.08)	1	(1, 1, 1)	0.9863	1.997	0	1.0000
		304.40 (302.33)	2	(1, 1, 1)	0.9863	1.994	1	1.0000
		304.89 (302.83)	2	(1, 1, 1)	0.9863	2.000	2	1.0000
314.48	1	314.50 (313.20)	1	(1, 1, 1)	0.9831	0.014	0	1.0000

Table 2 Properties of computed TR eigenstates for $HF@C_{60}$

$\Delta E_0/\mathrm{cm}^{-1}$	g_0	$\Delta E_P/\mathrm{cm}^{-1}$	g_P	(n,l,j)	$P_I(n,l,j)$	$\langle\lambda\rangle$	$\lvert m_\lambda\rvert$	$P_I(\lvert m_\lambda\rvert)$
0.00	1	0.00	1	(0, 0, 0)	0.9343	0.006	0	1.0000
33.70	3	31.26	1	(0, 0, 1)	0.8264	1.002	0	1.0000
		34.98	2	(0, 0, 1)	0.8128	1.001	1	0.9999
76.35	3	76.24	1	(1, 1, 0)	0.7850	1.002	0	1.0000
		76.42	2	(1, 1, 0)	0.7721	1.002	1	1.0000
90.76	5	89.17	1	(1, 1, 1)	0.5940	1.996	0	0.9999
		89.93	2	(1, 1, 1)	0.5991	1.996	1	0.9997
		92.38	2	(1, 1, 1)	0.6020	2.001	2	0.9997
108.14	1	108.18	1	(1, 1, 1)	0.7182	0.065	0	0.9999
109.00	3	108.40	2	(1, 1, 1)	0.9559	1.018	1	1.0000
		110.36	1	(1, 1, 1)	0.9682	1.001	0	0.9999
123.56	5	122.33	1	(0, 0, 2)	0.6242	1.993	0	0.9999
		123.01	2	(0, 0, 2)	0.6248	1.996	1	0.9999
		125.02	2	(0, 0, 2)	0.6364	2.001	2	0.9999
153.99	1	154.04	1	(2, 0, 0)	0.6112	0.680	0	1.0000
153.99	5	153.82	1	(2, 2, 0)	0.5228	1.763	0	1.0000
		153.94	2	(2, 2, 0)	0.6356	2.001	1	0.9999
		154.17	2	(2, 2, 0)	0.6187	2.001	2	0.9999
154.74	4	153.49	1	(2, 2, 1)	0.5005	2.997	0	0.9919
156.01	3	154.16	2	(2, 2, 1)	0.5056	2.995	1	0.7051
		155.48	2	(2, 2, 1)	0.5279	2.993	2	0.7051
		156.53	1	(2, 2, 1)	0.5086	3.001	3	0.9999
		157.66	1	(2, 2, 1)	0.5344	3.001	3	0.9918

This journal is © The Royal Society of Chemistry [year]

Table 3 Properties of computed TR eigenstates for $H_2O@C_{60}$

$\Delta E_0/\mathrm{cm}^{-1}$	g_0	$\Delta E_P/\mathrm{cm}^{-1}$	g_P	$(n,l,j_{k_a k_c})$	$P_l(n,l,j_{k_a k_c})$	$\langle\lambda\rangle$	$\lvert m_\lambda\rvert$	$P_l(\lvert m_\lambda\rvert)$
para:								
0.00	1	0.00	1	$(0,0,0_{0,0})$	0.9698	0.012	0	1.0000
36.61	3	36.47	2	$(0,0,1_{1,1})$	0.9597	1.006	1	1.0000
		36.84	1	$(0,0,1_{1,1})$	0.9629	1.001	0	1.0000
69.89	5	67.90	1	$(0,0,2_{0,2})$	0.8702	1.999	0	1.0000
		68.88	2	$(0,0,2_{0,2})$	0.8739	2.001	1	1.0000
		72.23	2	$(0,0,2_{0,2})$	0.8798	2.001	2	1.0000
94.71	5	94.74	1	$(0,0,2_{1,1})$	0.9643	2.001	0	1.0000
		94.89	2	$(0,0,2_{1,1})$	0.9637	2.001	2	0.9990
		94.99	2	$(0,0,2_{1,1})$	0.9605	1.998	1	0.9990
133.95	5	131.79	2	$(0,0,2_{2,0})$	0.8323	2.002	2	1.0000
		135.15	2	$(0,0,2_{2,0})$	0.8259	2.001	1	1.0000
		136.32	1	$(0,0,2_{2,0})$	0.8238	2.000	0	1.0000
140.57	4	138.52	1	$(0,0,3_{1,3})$	0.9162	3.000	0	0.9960
141.80	3	139.58	2	$(0,0,3_{1,3})$	0.9162	3.000	1	0.8743
		141.33	2	$(0,0,3_{1,3})$	0.9161	3.000	2	0.8742
		143.59	1	$(0,0,3_{1,3})$	0.9177	3.000	3	1.0000
		144.69	1	$(0,0,3_{1,3})$	0.9171	3.001	3	0.9960
172.67	3	172.54	2	$(1,1,0_{0,0})$	0.9338	1.004	1	1.0000
		172.95	1	$(1,1,0_{0,0})$	0.9385	1.004	0	1.0000
ortho:								
23.75	3	21.02	1	$(0,0,1_{0,1})$	0.9707	1.002	0	1.0000
		25.24	2	$(0,0,1_{0,1})$	0.9704	1.002	1	1.0000
41.94	3	40.60	2	$(0,0,1_{1,0})$	0.9624	1.005	1	1.0000
		44.73	1	$(0,0,1_{1,0})$	0.9648	1.002	0	1.0000
78.72	5	76.90	1	$(0,0,2_{1,2})$	0.9585	2.001	0	1.0000
		77.96	2	$(0,0,2_{1,2})$	0.9558	1.999	1	1.0000
		80.70	2	$(0,0,2_{1,2})$	0.9578	2.002	2	1.0000
132.67	5	130.68	2	$(0,0,2_{2,1})$	0.9210	2.004	2	0.9999
		133.74	2	$(0,0,2_{2,1})$	0.8724	2.065	1	0.9983
		134.80	1	$(0,0,2_{2,1})$	0.9229	2.000	0	1.0000
135.59	3	134.26	2	$(0,0,3_{0,3})$	0.5964	2.954	1	0.9526
136.64	4	134.34	1	$(0,0,3_{0,3})$	0.6257	3.000	0	0.9943
		136.53	2	$(0,0,3_{0,3})$	0.6314	2.999	2	0.9510
		138.78	1	$(0,0,3_{0,3})$	0.6348	3.000	3	0.9943
		139.67	1	$(0,0,3_{0,3})$	0.6380	3.000	3	1.0000
172.86	3	172.43	1	$(0,0,3_{1,2})$	0.9300	3.000	0	0.9998
172.89	4	172.59	2	$(0,0,3_{1,2})$	0.9314	3.000	1	0.9990
		173.08	2	$(0,0,3_{1,2})$	0.9305	3.000	2	0.9989
		173.77	1	$(0,0,3_{1,2})$	0.9337	3.001	3	0.9999
		173.81	1	$(0,0,3_{1,2})$	0.9320	3.000	3	0.9999
193.35	3	191.79	2	$(1,1,1_{0,1})$	0.9325	1.206	1	1.0000
		194.77	1	$(1,1,1_{0,1})$	0.9321	1.002	0	1.0000
197.36	5	195.61	1	$(1,1,1_{0,1})$	0.9369	1.922	0	1.0000
		197.75	2	$(1,1,1_{0,1})$	0.9338	1.866	1	1.0000
		198.79	2	$(1,1,1_{0,1})$	0.9332	2.001	2	1.0000
202.71	1	203.29	1	$(1,1,1_{0,1})$	0.9717	0.303	0	1.0000

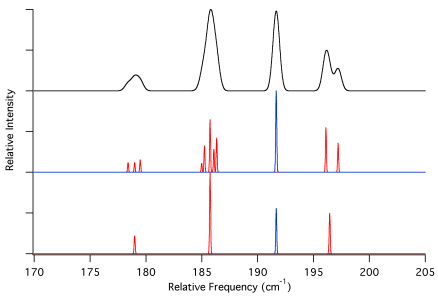

Fig. 1 Simulated $v = 0 \rightarrow 1$ near-IR absorption spectra of $H_2@C_{60}(s)$. Bottom: Spectra for the H orientation for *para* (blue) and *ortho* (red) H_2 at 0.1 cm^{-1} resolution. Middle: Same as bottom except for the P orientation. Top: Spectrum computed for a 15% contribution from the H orientation and 85% from the P at 0.7 cm^{-1} resolution. In all the spectra the *ortho*/*para* population ratio was taken to be 3:1 and the temperature was taken to be 6 K.

In the measured FIR spectrum of $HF@C_{60}(s)$ (Fig. 3a-bottom from Krachmalnicoff *et al.*[9]) two bands are observed at about 33 and 78.6 cm^{-1}, respectively, with the former split by about 3.9 cm^{-1} and the latter unsplit. The 33 cm^{-1} band is assigned in that work to the set of $|n,l,j\rangle = |0,0,0\rangle \rightarrow |0,0,1\rangle$ rotational transitions, and its splitting is taken as evidence for symmetry breaking. The 78.6 cm^{-1} band is assigned as the translational fundamental $|n,l,j\rangle = |0,0,0\rangle \rightarrow |1,1,0\rangle$. Figure 2 shows our simulated FIR spectra for $HF@C_{60}(s)$. The frequency range shown contains all the features that are computed to have significant intensity. The bottom trace corresponds to the H crystal orientation at 0.2 cm^{-1} resolution. The middle spectrum is that for the P orientation at the same resolution. The upper spectrum is a weighted sum of the H and P spectra (0.15H + 0.85P) at 2.0 cm^{-1} resolution. Comparison with experiment reveals that the top spectrum is indeed a good match for the measured results. Hence, the quadrupole model predicts the observed split band quantitatively and also predicts the lack of any observable splitting for the band that is unsplit in the experimental spectrum. Notably, the assignments for the bands in the simulated spectra confirm the ones made by Krachmalnicoff *et al.*[9] As such, the lack of an appreciable splitting of the translational fundamental is easily understood within the electrostatic/quadrupole model, as we discuss above.

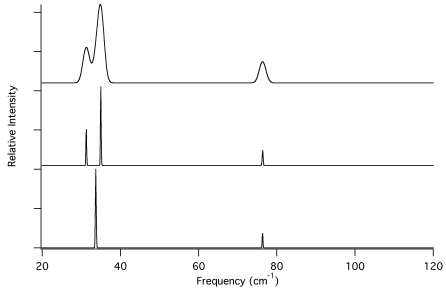

Fig. 2 Simulated far-IR absorption spectra of $HF@C_{60}(s)$. Bottom: Spectra for the H orientation at 0.2 cm^{-1} resolution. Middle: Same as bottom except for the P orientation. Top: Spectrum computed for a 15% contribution from the H orientation and 85% from the P at 2.0 cm^{-1} resolution. In all the spectra the temperature was taken to be 5 K.

The appreciable FIR intensity of the translational fundamental is not something that would be expected for transitions induced by the permanent dipole of the HF moiety: The diatomic rotational selection rule $|\Delta j| = 1$ should apply. The fact that it does appear in the simulations at an intensity that is a significant fraction of that for the 33 cm^{-1} band is due to translation-rotation coupling. That is, while the computed ground state is about 93% $|0,0,0\rangle$ it also has a 6% contribution from $|1,1,1\rangle$, which has nonzero dipole matrix elements with the $|1,1,0\rangle$ states. Similarly, the computed states of the translationallly excited level, while predominantly $|1,1,0\rangle$, have $\sim$ 15% contributions from $|0,0,1\rangle$ states, and the latter are dipole-connected with $|0,0,0\rangle$. It is presumably this mechanism that lends intensity to the translational fundamental in the measured FIR spectrum.

Finally, we present in Fig. 3 the FIR spectra simulated for $H_2O@C_{60}(s)$. The spectral region shown contains all of the features with appreciable intensity in the spectrum at frequencies less than 200 cm^{-1}, apart from ones in the 170–180 cm^{-1} range that are more than an order of magnitude less intense than those in the figure. The lower spectrum corresponds to the H crystal orientation at 0.2 cm^{-1} resolution. The *para* contribution to the spectrum is in blue and the *ortho* is in red. The middle spectrum is analogous, but for the P orientation. The top spectrum is 0.15H + 0.85P at 1.0 cm^{-1} resolution and is meant to be indicative of what might be measured in an experiment. In each case the *ortho*/*para* population ratio is taken to be 3:1 and the relative populations of the *ortho* initial states (those of the 1_{01} level – see Table 3) are taken to conform to a 5-Kelvin Boltzmann distribution. The three gross features in each spectrum, in order of increasing frequency, correspond to the $1_{01} \rightarrow 1_{10}$, $0_{00} \rightarrow 1_{11}$ and $1_{01} \rightarrow 2_{12}$ rotational bands. One sees from the spectra that the electrostatic model predicts significant splitting of the two *ortho* bands for species in the P orientation and that these splittings could well be observable in an FIR experiment with high-enough resolution. The results of such an experiment could thus prove an excellent test of the electrostatic model.

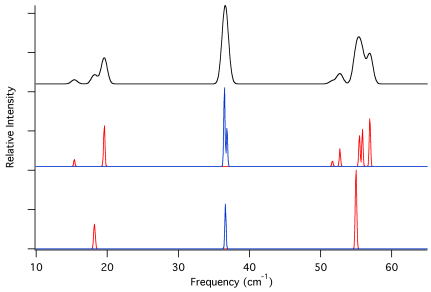

Fig. 3 Simulated far-IR absorption spectra of $H_2O@C_{60}(s)$. Bottom: Spectra for the H orientation for *para* (blue) and *ortho* (red) H_2O at 0.2 cm^{-1} resolution. Middle: Same as bottom except for the P orientation. Top: Spectrum computed for a 15% contribution from the H orientation and 85% from the P at 1.0 cm^{-1} resolution. In all the spectra the *ortho*/*para* population ratio was taken to be 3:1 and the temperature was taken to be 5 K.

One last point regarding the M = H_2O spectra relates to the weak features computed to be in the 170–180 cm^{-1} range. These

This journal is © The Royal Society of Chemistry [year]

correspond to $\Delta n = 1$ translational transitions and are analogous to the higher frequency band in the HF@$C_{60}(s)$ FIR spectra. Just as for M = HF, these features gain intensity by translation-rotation mixing. However, the extent of such mixing for the relevant M = H_2O states is considerably less than for the M = HF states. As a result the intensities of the translational features relative to the rotational ones for H_2O are much smaller than for HF.

4 Conclusions

We have investigated the effects of the symmetry breaking on the excited TR eigenstates of the endofullerenes M@$C_{60}(s)$ (M = H_2, HF, H_2O), as well as its manifestations in the simulated near-IR (NIR) and far-IR (FIR) spectra of these species. This extends our earlier study focused on the symmetry-breaking induced splittings of the three-fold degenerate ground states of the endohedral *ortho*-H_2, *ortho*-H_2O and the $j = 1$ level of HF.[41] Our approach towards calculating the TR eigenstates of M inside the C_{60} cage embedded in $C_{60}(s)$ has been reported previously.[41]

The TR eigenstates have been calculated variationally for the endohedral M = H_2, HF, and H_2O, and for both the P and H crystal orientations. However, for the H orientation, the calculated quadrupole-induced splittings are less than 0.1 cm^{-1} for all the TR states of these species, and therefore these states are very close to those of the corresponding isolated M@C_{60} (no quadrupolar interaction). The reason for this was discussed earlier.[41] Therefore, only the P-orientation results are presented in detail and discussed. For the P orientation, the splittings calculated in this work for the ground states of the endohedral *ortho*-H_2, *ortho*-H_2O and the $j = 1$ level of HF (1.09 cm^{-1}, 4.22 cm^{-1}, and 3.72 cm^{-1}, respectively) are, of course, the same as those reported previously.[41] They are in excellent agreement with the splittings measured for these levels, as well as the 1:2 degeneracy pattern of the split states.

For excited TR levels of the three species considered, the splittings differ greatly depending on the nature of the excitations involved. In each of the species, the splittings computed for higher rotationally excited levels are similar in magnitude to those for the $j = 1$ levels. However, for the levels that are excited purely translationally, the calculated splittings are about an order of magnitude smaller than those of the purely rotational ones. This is true for all three species. Thus, the splittings of the $|1,1,0\rangle$ levels in M = H_2, HF, and H_2O are only 0.04 cm^{-1}, 0.18 cm^{-1} and 0.41 cm^{-1}, respectively. The splitting magnitudes are similarly small for the $n = 2, j = 0$ levels. This drastic difference between the splittings of excited levels that have some rotational excitation and ones that do not can be readily understood in the context of the electrostatic/quadrupole model.

Analysis of the low-energy TR eigenstates of the three species reveals that the total angular momentum quantum number λ is close to an integer for virtually all the states, as is $|m_\lambda|$. This means that even under the symmetry-breaking quadrupolar M-NN interaction, λ and $|m_\lambda|$ largely remain good quantum numbers, and can be used to label the TR eigenstates. The situation is less uniform with regard to the quantum numbers n, l, j for M = H_2 and HF, and $n, l, j_{k_a k_c}$ for M = H_2O. In the case of M = H_2 and H_2O, these quantum numbers are very good, since for H_2 the lower-energy TR eigenstates have $P_l(n,l,j)$ values very close to 1, and for H_2O, $P_l(n,l,j_{k_a k_c})$ is almost always greater than 0.8 or 0.9. However, for the TR eigenstates of M = HF, $P_l(n,l,j)$ is mostly in the range 0.5-0.6. Consequently, the goodness of the quantum numbers n, l, j is much lower for HF than for H_2, most likely because of the large mass asymmetry of HF.

The low-temperature (5-6 K) NIR and FIR spectra of the three species are simulated using the computed TR eigenstates, for the purpose of comparison with the experimental spectra. For M = HF and H_2O, the FIR spectra of each species are simulated separately for the P and H orientations (and for *ortho*- and *para*-H_2O), and also combined as their weighted sum, 0.15H + 0.85P. For M = HF, the weighted-sum FIR spectrum reproduces very well the measured spectrum, matching quantitatively both the observed split band and the absence of splitting for the band that is unsplit in the experimental spectrum. For M = H_2O, the 0.15H + 0.85P combined FIR spectrum predicts features that could be observed in an FIR experiment, providing an excellent test of the electrostatic model. For M = H_2, the NIR spectra of the combination bands built off the H_2 intramolecular vibrational fundamental are simulated for the P and H orientations (and for *ortho*- and *para*-H_2). The simulated weighted-sum (0.15H + 0.85P) spectrum reproduces the qualitative features of the measured NIR spectrum, in particular the conspicuous splitting of one of the bands ($\lambda' = 0$).

Our theoretical investigations of the symmetry breaking in the solid light-molecule endofullerenes M@C_{60} (M = H_2, H_2O, HF) reported in this paper and the previous one[41] have yielded a number of results that are potentially observable spectroscopically, and can serve as the test of our electrostatic model and its predictions. We hope that this will stimulate further experimental and theoretical studies of these unique systems that have both fundamental and possibly practical significance.

Conflicts of Interest

There are no conflicts of interest to declare.

Acknowledgements

Z.B. and D.N. are grateful to the National Science Foundation for its partial support of this research through Grants CHE-1566085 and DMR/BSF-1611382, respectively.

References

1 H. W. Kroto, J. R. Heath, S. C. O'Brien, R. F. Curl and R. E. Smaley, *Nature*, 1985, **318**, 162.
2 M. H. Levitt, *Phil. Trans. R. Soc. A*, 2013, **371**, 20120429.
3 Y. Rubin, *Chem. Eur. J.*, 1997, **3**, 1009.
4 Y. Rubin, *Top. Curr. Chem.*, 1999, **199**, 67.
5 Y. Rubin, T. Jarrosson, G. W. Wang, M. D. Bartberger, K. N. Houk, G. Schick, M. Saunders and R. J. Cross, *Angew. Chem. Int. Ed.*, 2001, **40**, 1543.
6 K. Komatsu, M. Murata and Y. Murata, *Science*, 2005, **307**, 238.

7 M. Murata, Y. Murata and K. Komatsu, *J. Am. Chem. Soc.*, 2006, **128**, 8024.

8 K. Kurotobi and Y. Murata, *Science*, 2011, **333**, 613.

9 A. Krachmalnicoff, R. Bounds, S. Mamone, S. Alom, M. Concistrè, B. Meier, K. Kouřil, M. E. Light, M. R. Johnson, S. Rols, A. J. Horsewill, A. Shugai, U. Nagel, T. Rõõm, M. Carravetta, M. Levitt and R. J. Whitby, *Nature Chem.*, 2016, **8**, 953.

10 M. Murata, S. Maeda, Y. Morinaka, Y. Murata and K. Komatsu, *J. Am. Chem. Soc.*, 2008, **130**, 15800.

11 R. Zhang, M. Murata, T. Aharen, A. Wakamiya, T. Shimoaka, T. Hasegawa and Y. Murata, *Nature Chem.*, 2016, **8**, 435.

12 R. Zhang, M. Murata, A. Wakamiya, T. Shimoaka, T. Hasegawa and Y. Murata, *Sci. Adv.*, 2017, **3**, e1602833.

13 M. Xu, F. Sebastianelli, Z. Bačić, R. Lawler and N. J. Turro, *J. Chem. Phys.*, 2008, **128**, 011101.

14 P. M. Felker and Z. Bačić, *J. Chem. Phys.*, 2016, **144**, 201101.

15 P. R. Bunker and P. Jensen, *Molecular Symmetry and Spectroscopy, E-book edition*, NRC Research Press, Ottawa, Ontario, Canada, 2006.

16 M. H. Levitt and A. J. Horsewill, *Phil. Trans. R. Soc. A*, 2013, **371**, 20130124.

17 M. Xu, F. Sebastianelli, Z. Bačić, R. Lawler and N. J. Turro, *J. Chem. Phys.*, 2008, **129**, 064313.

18 M. Xu, F. Sebastianelli, B. R. Gibbons, Z. Bačić, R. Lawler and N. J. Turro, *J. Chem. Phys.*, 2009, **130**, 224306.

19 S. Mamone, M. Ge, D. Hüvonen, U. Nagel, A. Danquigny, F. Cuda, M. C. Grossel, Y. Murata, K. Komatsu, M. H. Levitt, T. Rõõm and M. Carravetta, *J. Chem. Phys.*, 2009, **130**, 081103.

20 P. M. Felker and Z. Bačić, *J. Chem. Phys.*, 2016, **145**, 084310.

21 M. Xu, S. Ye, R. Lawler, N. J. Turro and Z. Bačić, *Phil. Trans. R. Soc. A*, 2013, **371**, 20110630.

22 M. Xu, S. Ye, A. Powers, R. Lawler, N. J. Turro and Z. Bačić, *J. Chem. Phys.*, 2013, **139**, 064309.

23 A. J. Horsewill, S. Rols, M. R. Johnson, Y. Murata, M. Murata, K. Komatsu, M. Carravetta, S. Mamone, M. H. Levitt, J. Y. C. Chen, J. A. Johnson, X. Lei and N. J. Turro, *Phys. Rev. B*, 2010, **82**, 081410(R).

24 A. J. Horsewill, K. S. Panesar, S. Rols, J. Ollivier, M. R. Johnson, M. Carravetta, S. Mamone, M. H. Levitt, Y. Murata, K. Komatsu, J. Y. C. Chen, J. A. Johnson, X. Lei and N. J. Turro, *Phys. Rev. B*, 2012, **85**, 205440.

25 A. J. Horsewill, K. Goh, S. Rols, J. Ollivier, M. R. Johnson, M. H. Levitt, M. Carravetta, S. Mamone, Y. Murata, J. Y. C. Chen, J. A. Johnson, X. Lei and N. J. Turro, *Phil. Trans. R. Soc. A*, 2013, **371**, 20110627.

26 S. Mamone, M. Jiménez-Ruiz, M. R. Johnson, S. Rols and A. J. Horsewill, *Phys. Chem. Chem. Phys.*, 2016, **18**, 29369.

27 M. Ge, U. Nagel, D. Hüvonen, T. Rõõm, S. Mamone, M. H. Levitt, M. Carravetta, Y. Murata, K. Komatsu, J. Y. C. Chen and N. J. Turro, *J. Chem. Phys.*, 2011, **134**, 054507.

28 M. Ge, U. Nagel, D. Hüvonen, T. Rõõm, S. Mamone, M. H. Levitt, M. Carravetta, Y. Murata, K. Komatsu, X. Lei and N. J. Turro, *J. Chem. Phys.*, 2011, **135**, 114511.

29 T. Rõõm, L. Peedu, M. Ge, D. Hüvonen, U. Nagel, S. Ye, M. Xu, Z. Bačić, S. Mamone, M. Levitt, M. Carravetta, J. Y. C. Chen, X. Lei, N. J. Turro, Y. Murata and K. Komatsu, *Phil. Trans. R. Soc. A*, 2013, **371**, 20110631.

30 Y. N. Kalugina and P. N. Roy, *J. Chem. Phys.*, 2017, **147**, 244303.

31 M. Xu, L. Ulivi, M. Celli, D. Colognesi and Z. Bačić, *Phys. Rev. B*, 2011, **83**, 241403(R).

32 M. Xu and Z. Bačić, *Phys. Rev. B*, 2011, **84**, 195445.

33 M. Xu, L. Ulivi, M. Celli, D. Colognesi and Z. Bačić, *Chem. Phys. Lett.*, 2013, **563**, 1.

34 M. Xu, M. Jiménez-Ruiz, M. R. Johnson, S. Rols, S. Ye, M. Carravetta, M. S. Denning, X. Lei, Z. Bačić and A. J. Horsewill, *Phys. Rev. Lett.*, 2014, **113**, 123001.

35 M. Xu, S. Ye and Z. Bačić, 2015, **6**, 3721.

36 B. Poirier, *J. Chem. Phys.*, 2015, **143**, 101104.

37 Y. Kohama, T. Rachi, J. Jing, Z. Li, J. Tang, R. Kumashiro, S. Izumisawa, H. Kawaji, T. Atake, H. Sawa, Y. Murata, K. Komatsu and K. Tanigaki, *Phys. Rev. Lett.*, 2009, **103**, 073001.

38 S. Mamone, M. R. Johnson, J. Ollivier, S. Rols, M. H. Levitt and A. J. Horsewill, *Phys. Chem. Chem. Phys.*, 2016, **18**, 1998.

39 C. Beduz, M. Carravetta, J. Y. C. Chen, M. Concistre, M. Denning, M. Frunzi, A. J. Horsewill, O. G. Johannessenn, R. Lawler, X. Lei, M. H. Levitt, Y. Li, S. Mamone, Y. Murata, U. Nagel, T. Nishida, J. Ollivier, S. Rols, T. Rõõm, R. Sarkar, N. J. Turro and Y. Yang, *Proc. Natl. Acad. Sci. U.S.A.*, 2012, **109**, 12894.

40 K. S. K. Goh, M. Jiménez-Ruiz, M. R. Johnson, S. Rols, J. Ollivier, M. S. Denning, S. Mamone, M. H. Levitt, X. Lei, Y. Li, N. J. Turro, Y. Murata and A. J. Horsewill, *Phys. Chem. Chem. Phys.*, 2014, **16**, 21330.

41 P. M. Felker, V. Vlček, I. Hietanen, S. FitzGerald, D. Neuhauser and Z. Bačić, *Phys. Chem. Chem. Phys.*, 2017, **19**, 31274.

42 W. I. F. David, R. M. Ibberson, T. J. S. Dennis, J. P. Hare and K. Prassides, *Europhys. Lett.*, 1992, **18**, 219.

43 W. I. F. David, R. M. Ibberson, J. C. Matthewman, K. Prassides, T. J. S. Dennis, J. P. Hare, H. W. Kroto, R. Taylor and D. R. M. Walton, *Nature*, 1991, **353**, 147.

44 A. B. Farimani, Y. Wu and N. R. Aluru, *Phys. Chem. Chem. Phys.*, 2013, **15**, 17993.

45 R. Sachidanandam and A. B. Harris, *Phys. Rev. Lett.*, 1991, **67**, 1467.

46 A. B. Harris and R. Sachidanandam, *Phys. Rev. B*, 1992, **46**, 4944.

47 V. A. Mandelshtam and H. S. Taylor, *Phys. Rev. Lett.*, 1997, **78**, 3274.

48 M. R. Wall and D. Neuhauser, *J. Chem. Phys.*, 1995, **102**, 8011.

This journal is © The Royal Society of Chemistry [year]